



19 **Abstract**

20 Real-time probabilistic flood inundation mapping is crucial for flood risk warning and decision
21 making during the emergency of an upcoming flood event. Considering high uncertainties
22 involved in the modeling of a nonlinear and complex flood event, providing a deterministic flood
23 inundation map can be erroneous and misleading for reliable and timely decision making. The
24 conventional flood hazard maps provided for different return periods cannot also represent the
25 actual dynamics of flooding rivers. Therefore, a real-time modeling framework that forecasts the
26 inundation areas before the onset of an upcoming flood is of paramount importance. Sequential
27 Data Assimilation (DA) techniques are well-known for real-time operation of physical models
28 while accounting for existing uncertainties. In this study, we present a Data Assimilation (DA)-
29 hydrodynamic modeling framework where multiple gauge observations are integrated into the
30 LISFLOOD-FP model to improve its performance. This study utilizes the Ensemble Kalman Filter
31 (EnKF) in a multivariate fashion for dual estimation of model state variables and parameters where
32 the correlations among point source observations are taken into account. First, a synthetic
33 experiment is designed to assess the performance of the proposed approach, then the method is
34 used to simulate the Hurricane Harvey flood in 2017. Our results indicate that the multivariate
35 assimilation of point-source observations into hydrodynamic models can improve the accuracy
36 and reliability of probabilistic flood inundation mapping by 5-7% while it also provides the basis
37 for sequential updating and real-time flood inundation mapping.

38 **Keywords:** Data Assimilation; Probabilistic Flood Inundation Mapping; Hydrodynamic Model;
39 Ensemble Kalman Filter

40

41

42

43

44

45



46 **1. Introduction**

47 The on-time, accurate, and reliable characterization of an upcoming flood event is imperative for
48 proper decision making and risk analysis. A well-calibrated hydrologic model coupled with
49 reliable weather forecast models can be used to generate the streamflow forecast (Clark and Hay,
50 2004; Cuo et al., 2011; Habets et al., 2004). While streamflow forecasting during flood events is
51 indispensable, the critical step for flood risk analysis is to estimate the flood inundation areas
52 corresponding to the forecasted streamflow of a potential upcoming event. Hydrodynamic models
53 are common tools used to simulate the physics of a river system and predict the spatiotemporal
54 distribution of water surface elevation. The predicted water surface elevation can be simply
55 converted to water depth and inundation area by overlaying with a high-resolution Digital
56 Elevation Model (DEM) (Merwade et al., 2008; Teng et al., 2017).

57 According to the literature, most studies have analyzed the flood events for which the flood extent
58 maps were available from surveying or satellite remote sensing. These studies include but are not
59 limited to, calibration and assimilation of hydrodynamic models (Baldassarre et al., 2009; García-
60 Pintado et al., 2013; Gobeyn et al., 2017; Hostache et al., 2009; Lai et al., 2014; Pappenberger et
61 al., 2007; Rahman and Thakur, 2018; Tarpanelli et al., 2013). Depending on the research
62 objectives, such studies are crucial as they address important theoretical questions and advance the
63 flood modeling task. For example, several studies have used satellite remote sensing data, such as
64 Synthetic Aperture Radar (SAR) images, to find the sensitivity of hydrodynamic models to their
65 parameters, compare calibration strategies and test the application of assimilating remote sensing
66 data into these models (Di Baldassarre et al., 2009; Hunter et al., 2005; Mason et al., 2009; Matgen
67 et al., 2010). Since floods happen in a short period and at a certain location, it is most often not
68 possible to find an appropriate remote sensing image that covers those inundated areas during the



69 flood period. This is the main reason that research on flood inundation mapping is mostly limited
70 to post-event analysis where specific study areas with available remote sensing data are used as
71 testbeds.

72 Federal Emergency Management Agency (FEMA) is the leading agency in the United States that
73 provides flood hazard and risk maps over the Contiguous United States (CONUS). These maps
74 display the flood-prone areas corresponding to specific return periods (e.g. 100 and 500-year
75 events). While the FEMA flood hazard and risk maps provide general information about risk areas,
76 they are not always reliable for an upcoming flood event with different return periods. For
77 example, FEMA 100-year and 500-year flood hazard maps covered only one-third and half of the
78 inundated areas induced by Hurricane Harvey in Harris County, Texas, respectively (Pinter et al.,
79 2017). The National Water Center Innovators Program proposed the idea of real-time flood
80 inundation mapping across the United States in 2015 (Maidment, 2017). It highlighted the
81 importance of event-based flood inundation mapping where a model uses the forecasted river
82 discharge to estimate the inundation areas corresponding to a specific flood just before the onset
83 of the event. Compared to the traditional flood hazard mapping, real-time flood inundation
84 mapping is more informative and beneficial for emergency response-related decision-making.

85 In real-time flood inundation mapping, the model takes advantage of forecasted forcing data and
86 generates inundation areas corresponding to an upcoming flood event. Providing these maps ahead
87 of time is extremely valuable for building a robust flood warning system. Data assimilation (DA)
88 is an effective approach commonly used to improve the performance of real-time hydrologic
89 forecasting by updating the model state variables and parameters when new observation becomes
90 available (Moradkhani et al., 2019). The integration of DA with physical models is highly
91 advantageous as it enables accounting for different sources of uncertainties involved in model



92 predictions. These include (1) forcing data uncertainty due to the limitation of measurements and
93 spatiotemporal representativeness of the data (Alemohammad et al., 2015; Kumar et al., 2017), (2)
94 parameter uncertainty due to equifinality and non-uniqueness of parameters (Abbaszadeh et al.,
95 2018; Leach et al., 2018), (3) model structural uncertainty due to the imperfect representation and
96 conceptualization of a real system (Abbaszadeh et al., 2019; Pathiraja et al., 2018; Zhang et al.,
97 2019) and (4) initial and boundary condition uncertainty (DeChant and Moradkhani, 2014; Lee et
98 al., 2011).

99 Probabilistic forecasting and uncertainty quantification using DA have been the core of modeling
100 in the atmospheric and oceanic sciences (e.g. Anderson and Anderson, 1999; Courtier et al., 1993).
101 Later, the hydrologic community started to utilize this approach to account for the uncertainties
102 involved in different layers of model predictions and provide more accurate and reliable model
103 estimates such as soil moisture (Pauwels et al., 2001; Reichle et al., 2002), streamflow
104 (Moradkhani et al., 2005a; Vrugt et al., 2006), snow (Sheffield et al., 2003; Slater and Clark, 2006)
105 and so many other variables. Despite these advances in hydrologic studies, the application of data
106 assimilation in conjunction with hydrodynamic models has received little attention in the literature.
107 The characterization of uncertainty in hydrodynamic models for probabilistic flood inundation
108 mapping has been mostly limited to conventional techniques, such as random Monte Carlo
109 sampling (Domeneghetti et al., 2013; Neal et al., 2013; Pedrozo-Acuña et al., 2015; Purvis et al.,
110 2008) and Generalized Likelihood Uncertainty Estimation (GLUE) (Aronica et al., 2002a;
111 Romanowicz and Beven, 2003).

112 The effectiveness and application of assimilating remotely sensed data (e.g. Soil Moisture Active
113 Passive (SMAP)) into hydrologic models have been vastly investigated in the literature
114 (Abbaszadeh et al., 2020; Azimi et al., 2020; Lievens et al., 2017). However, given the small scale



115 of the hydrodynamic modeling process, the spatiotemporal resolution of current satellite products
116 is not adequate for assimilating into these models. To properly estimate the flood inundation
117 extent, a spatial resolution less than river width (e.g. 100 m) is recommended. In addition, due to
118 the short duration of floods, satellite data with daily revisit time is needed. Since remote sensing
119 products do not provide such high spatiotemporal resolution data for hydrodynamic models, the
120 research on hydrodynamic data assimilation is limited in the literature. Due to the coarse spatial
121 resolution of satellites that provide water surface elevation data, some studies have limited their
122 analyses to large rivers with a width of above 1 km (e.g. study of Nile and Amazon) (Brêda et al.,
123 2019). However, since the width of the majority of rivers is less than 100 meters, these studies
124 cannot be practically used in many regions. Several studies used higher resolution synthetic
125 SWOT data to evaluate the performance of assimilation techniques (Durand et al., 2008; Munier
126 et al., 2015; Pedinotti et al., 2014; Yoon et al., 2012). While these works provided important
127 information about the assimilation of satellite data into hydrodynamic models, their applications
128 are only limited to synthetic experiments, making them impractical for real case studies. Some
129 studies have implemented indirect methods to estimate WSE from flood extents generated by high-
130 resolution SAR satellite data (Giustarini et al., 2011; Hostache et al., 2010; Matgen et al., 2010b;
131 Neal et al., 2009). This approach can provide high-resolution data that is suitable for the majority
132 of rivers. However, the reliability of this data is concerning because the methods used to convert
133 the flood extent to WSE pose additional errors which downgrades the quality of the final observed
134 data for assimilation practices. Besides these issues, the major drawback of remote sensing data
135 assimilation pertains to their coarse temporal resolutions. To efficiently monitor the flood
136 dynamics, the assimilation process should be performed at a daily/hourly time scale, however, the
137 revisit frequency of satellites used for capturing the water surface elevation ranges from a week to



138 a month. Therefore, there is a significantly low chance to capture multiple real-time remote sensing
139 images for the majority of inundated catchments during flood events. In the most optimistic
140 scenario, assimilation of satellite data is only limited to one/two updates during the simulation
141 period which may not be sufficient for reliable probabilistic flood inundation mapping.

142 Application of DA in hydrodynamic modeling can be either river monitoring or flood inundation
143 mapping. The goal of hydrodynamic data assimilation for river monitoring is to track variations in
144 the channel roughness and bathymetry in the long run. Therefore, the weekly/monthly satellite
145 data can be well assimilated into the models as the channel characteristics do not change on a daily
146 basis. On the other hand, flood inundation mapping needs an hourly/daily track of WSE because
147 floods happen rapidly and affect the river dynamics on a short time scale. The literature indicates
148 those studies that assimilated data into hydrodynamic models have been mostly designed for river
149 monitoring (Brêda et al., 2019; Durand et al., 2008; Yoon et al., 2012b). To capture the daily
150 dynamics of the rivers for real-time flood inundation mapping, the discharge and water stage
151 values measured at the gauge stations can be assimilated into the hydrodynamic models. Xu et al.,
152 (2017) performed a Particle Filtering (PF) approach to assimilate the water stage data from six
153 gauges into a hydrodynamic model. In order to calculate the particle weights in the filtering
154 process, they assumed that gauge observations are independent. In this study, however, we
155 consider interconnections among the gauge stations and apply multivariate Ensemble Kalman
156 Filter (EnKF) to a 2D hydrodynamic model for better characterization and quantification of
157 uncertainty and further improving the accuracy of model simulations.

158 Advancing the probabilistic hydrodynamic modeling with DA techniques is a necessary step to fill
159 the gap between hydrology and hydrodynamics. To address this problem, this study aims to
160 explore the capability of a standard sequential DA technique, namely the EnKF, for real-time



161 probabilistic flood inundation mapping. The past studies that used DA in conjunction with
162 hydrodynamic models have mostly focused on the quantification of uncertainty in one or two
163 hydrodynamic variables (e.g. Giustarini et al., (2011) and Hostache et al., (2018) only investigated
164 the uncertainty in the upstream flow and rainfall respectively; Yoon et al., (2012) focused on the
165 uncertainty of river bathymetry while ignoring the roughness parameter uncertainty). In addition,
166 the main application of DA-hydrodynamic modeling framework has been in river monitoring at
167 long-term or water stage forecasting during the flood events (Brêda et al., 2019; Matgen et al.,
168 2010; Xu et al., 2017). However, this study takes one step further and proposes a DA-
169 hydrodynamic modeling framework for real-time probabilistic flood inundation mapping while
170 accounting for all sources of uncertainties involved in the model simulations. These include
171 hydrodynamic model parameters (channel roughness and river bathymetry) uncertainty, forcing
172 data (river boundary conditions) uncertainty, and state variable (water depth) uncertainty.
173 Additionally, unlike past works that assimilated either discharge or water stage into the
174 hydrodynamic model, this study performs a multivariate DA to incorporate the observed values of
175 both variables into the hydrodynamic model for a reliable simulation of flooding and its
176 corresponding inundation area.

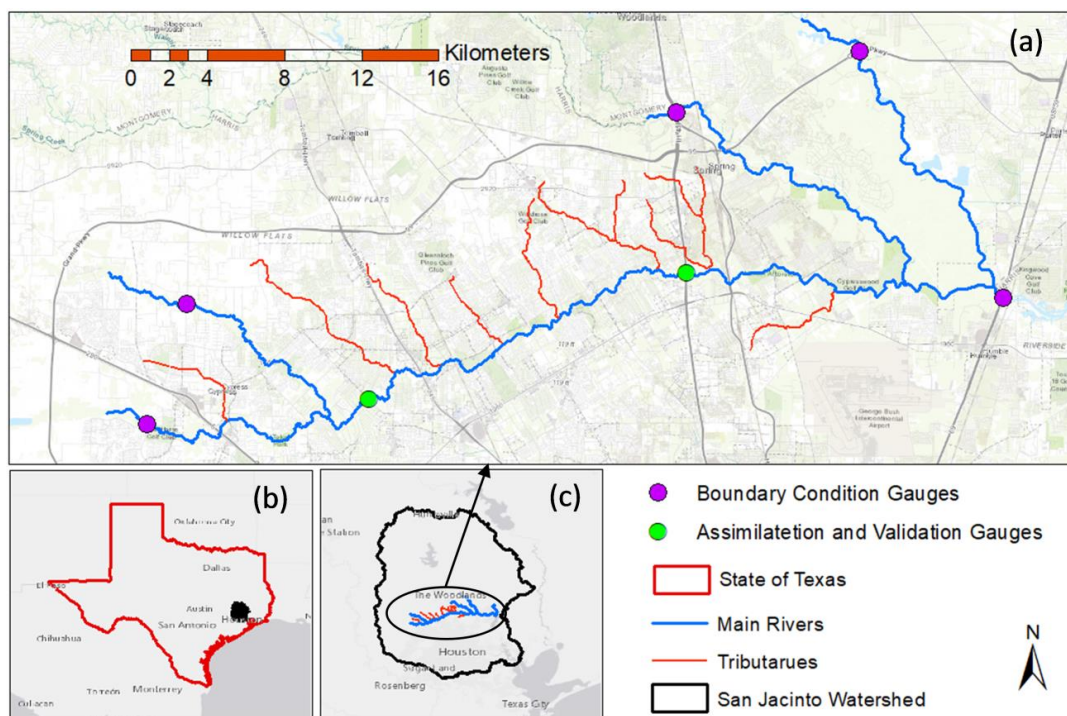
177 **2 Data and Study area**

178 In this study, we simulate the Hurricane Harvey flood, one of the worst natural disasters in the
179 history of the United States that caused more than 120 billion in damage
180 (https://www.nhc.noaa.gov/data/tcr/AL092017_Harvey.pdf). The Harvey storm hit Texas on
181 August 25, 2017, caused massive precipitation for six continuous days and resulted in extreme
182 flooding condition in Houston and surrounding areas. Given the considerable uncertainties in
183 hydrologic and hydrodynamic processes of such an extreme flood, a deterministic modeling



184 approach with fixed inputs provides erroneous simulations that are highly different from
185 observations. To account for the uncertainties involved in different layers of flood simulation, this
186 study implements a DA-hydrodynamic modeling framework and provides probabilistic flood
187 inundation maps.

188 Figure 1.a shows the study area that consists of four main channels (blue lines) and eight tributaries
189 (red lines). The upstream and downstream boundary conditions (purple points) are provided from
190 daily streamflow in four USGS gauges ((#08068090, # 08068500, #08068740, #08068780) and
191 water stage time series at the downstream gauge (#08069500). The daily streamflow discharge in
192 two internal gauges (green points #08068800 and #08069000) and water stage time series in the
193 second internal gauge are the observations that will be assimilated into the LISFLOOD-FP model.
194 Figures 1.b and 1.c present the geographic location of the study area within the state of Texas and
195 San Jacinto watershed, respectively. To set up the LISFLOOD-FP model, we use a DEM with 120
196 m spatial resolution. Such a coarse resolution DEM alleviates the computational intensity of the
197 proposed probabilistic hydrodynamic modeling framework. It should be noted that the subgrid
198 solver used for simulation of flood has the advantage of accepting narrow rivers with a width of
199 less than 120 m while the cell sizes are 120 m. In this study, the DA-hydrodynamic modeling
200 framework is parallelized and performed on the University of Alabama High-Performance
201 Computing (UAHPC) cluster.



202

203 *Figure 1 (a) Study area with all gauges, rivers, and tributaries. (b) Geographic location of San*
 204 *Jacinto Watershed within the state of Texas. (c) Geographic location of the study area within*
 205 *San Jacinto watershed (© Nhdplus and USGS).*

206 3. Methods

207 3.1 Flood inundation model

208 The flood inundation model used in this study is LISFLOOD-FP (Bates and De Roo, 2000), a
 209 raster-based 2D hydrodynamic model that simulates the spatiotemporal distribution of water
 210 surface elevation over the study area. The model solves the momentum and continuity equations
 211 (Saint Venont equations):

$$212 \frac{\partial Q}{\partial x} + \frac{\partial A}{\partial t} = 0 \quad (1)$$



$$213 \quad \frac{1}{A} \frac{\partial A}{\partial t} + \frac{1}{A} \frac{\partial \left(\frac{Q^2}{A} \right)}{\partial x} + g \frac{\partial h}{\partial x} - g(S_0 - S_f) = 0 \quad (2)$$

214 where Q is the flow rate at a given cross-section with the area of A in the main channel, x denotes
215 the location along the channel, t represents time, S_0 and S_f are channel bed and friction slopes, and
216 g is the gravitational acceleration.

217 We use the sub-gird channel solver, the most recently developed numerical scheme that considers
218 friction and water slope as well as local acceleration components in the shallow water equations
219 (Neal et al., 2012). This solver is advantageous for large-scale and efficient modeling as it utilizes
220 coarse resolution DEMs along with channel width values that are smaller than DEM resolution.
221 Since DA-hydrodynamic modeling requires hundreds of model simulations, a computationally
222 intensive operation, this solver helps reduce the computational burden and enables implementing
223 probabilistic flood inundation mapping within a DA framework. To set up the model, we assume
224 rectangular cross-section areas and a uniform roughness for both channel and floodplain. Given
225 the low sensitivity of LISFLOOD-FP to the floodplain roughness (Hall et al., 2005), this parameter
226 is assumed a constant value. However, the channel roughness is the only model roughness
227 parameter whose associated uncertainty is accounted for within the assimilation framework. We
228 also consider the uncertainty of bathymetry by defining an offset parameter that uniformly lowers
229 the DEM values of the river channels. In addition to model parameters (channel roughness and
230 bathymetry), the upstream and lateral fluxes entered the river system as the boundary conditions
231 of the model are other main sources of uncertainty in the assimilation framework.

232 The upstream boundary conditions are generated from four USGS gauge stations (Figure. 1). To
233 estimate the lateral fluxes, we calculate the deficit in the system as subtraction of the upstream
234 from downstream flows and then, distribute the deficit among river tributaries based on their



235 drainage areas (Please refer to Jafarzadegan et. al (2021) for detailed information about the
236 calculation of lateral flows in this study area). In section 3.3, we will further discuss the procedure
237 we used to initialize the model parameters and river boundary conditions.

238 **3.2 Ensemble Kalman Filter (EnKF)**

239 (Moradkhani et al., 2005b) provided a comprehensive description of the EnKF formulation for
240 dual estimation of state and parameters in hydrologic models. Here we briefly describe the EnKF
241 formulation for multivariate assimilation of point source water stage and discharge data into a
242 hydrodynamic model. For a more effective assimilation process, both types of interconnections
243 between observations, namely spatial correlation of a single observation (discharge or water stage)
244 among different gauges as well as the correlation between both observations at a single gauge are
245 taken into account in the EnKF equations. In this study, EnKF is used to simultaneously estimate
246 model states and parameters. For this purpose, the parameters should be treated similar to the state
247 variables with a difference that parameter evolution is generated artificially.

248 Let's assume a DA-hydrodynamic modeling framework with l parameters ($p = 1, 2, \dots, l$), m states
249 ($s = 1, 2, \dots, m$) and n observations ($j = 1, 2, \dots, n$). The following EnKF equations are described
250 in accordance with the flowchart shown in Figure 2. In the EnKF, parameter samples can be
251 generated by adding the noise of η_t with covariance Σ_t^θ to the prescribed parameters.

$$252 \quad \theta_{t+1}^{i-} = \theta_t^{i+} + \tau_t^i \quad \tau_t^i \sim N(0, \eta_{t+1}) \quad \forall \quad \eta_{t+1} = \Sigma_{t+1}^\theta \quad (3)$$

253 Using θ_{t+1}^{i-} and forcing data, a model state ensemble and predictions are generated, respectively.

$$254 \quad x_{t+1}^{i-} = f(x_t^{i+}, u_t^i, \theta_{t+1}^{i-}) + \omega_t^i \quad \omega_t^i \sim N(0, Q_t) \quad \forall \quad Q_t = \Sigma_t^x \quad (4)$$

$$255 \quad \hat{y}_{t+1}^i = h(x_{t+1}^{i-}, \theta_{t+1}^{i-}) + v_{t+1}^i \quad v_{t+1}^i \sim N(0, R_{t+1}) \quad \forall \quad R_{t+1} = \Sigma_{t+1}^y \quad (5)$$



256 where x_t , u_t , θ_t and y_t are the vector of the uncertain state variables, forcing data, model
 257 parameters and observation data at time step t , respectively. ω_t represents the model errors due to
 258 the imperfect model, and v_t is the measurement error. Most often, ω_t and v_t are assumed to be
 259 white noises with mean zero and covariance Q_t and R_t , respectively. In addition, the two noises
 260 ω_t and v_t are assumed to be independent.

261 Then we update the parameter ensemble members using the standard Kalman filter equation:

$$262 \quad \theta_{t+1}^{i+} = \theta_{t+1}^{i-} + K_{t+1}^{\theta} (y_{t+1}^i - \hat{y}_{t+1}^i) \quad (6)$$

263 where $K_{t+1}^{\theta} \in \mathbb{R}^{l \times n}$ is the Kalman gain matrix for correcting the parameter trajectories and is
 264 obtained by:

$$265 \quad K_{t+1}^{\theta} = \Sigma_{t+1}^{\theta y} [\Sigma_{t+1}^{yy} + R'_{t+1}]^{-1} \quad (7)$$

266 where $\Sigma_{t+1}^{\theta y} \in \mathbb{R}^{l \times n}$ is the cross-covariance matrix of parameter ensemble and prediction ensemble
 267 (Eq. 6). Unlike other studies, and for more realistic characterization of observation and model
 268 errors here the correlation between the errors associated with n observation data are accounted for
 269 during the assimilation process. Therefore, the covariance matrix $R'_t \in \mathbb{R}^{n \times n}$ is a nonzero matrix,
 270 such that the values in the diagonal represent the error associated with each observation data and
 271 all elements lower/upper the main diagonal denote the cross covariance between different
 272 observations (Eq. 7). $\Sigma_t^{yy} \in \mathbb{R}^{n \times n}$ is also a similar covariance matrix with the inclusion of error
 273 correlation between the model simulations (Eq. 8).

$$274 \quad \Sigma_{t+1}^{\theta y}(p, j) = \frac{1}{N} \sum_{i=1}^N [(\theta_{t+1}^{i-}(p) - E[\theta_{t+1}^-(p)]) (\hat{y}_{t+1}^i(j) - E[\hat{y}_{t+1}(j)])] \quad (8)$$

$$275 \quad R'_{t+1}(j, j') = \begin{cases} R_{t+1} & j = j' \\ \frac{1}{N} \sum_{i=1}^N [(y_{t+1}^i(j) - E[y_{t+1}(j)]) (y_{t+1}^i(j') - E[y_{t+1}(j')])] & j \neq j' \end{cases} \quad (9)$$



$$276 \quad \Sigma_{t+1}^{yy}(j, j') = \frac{1}{N} \sum_{i=1}^N [(\hat{y}_{t+1}^i(j) - E[\hat{y}_{t+1}(j)]) (\hat{y}_{t+1}^i(j') - E[\hat{y}_{t+1}(j')]))] \quad (10)$$

$$277 \quad E[\theta_{t+1}^-] = \frac{1}{N} \sum_{i=1}^N \theta_{t+1}^{i-} \quad (11)$$

$$278 \quad E[\hat{y}_{t+1}] = \frac{1}{N} \sum_{i=1}^N \hat{y}_{t+1}^i \quad (12)$$

279 Now using the updated parameter, the new model state trajectories (state forecasts) and prediction
 280 trajectories are generated:

$$281 \quad x_{t+1}^{i-} = f(x_t^{i+}, u_t^i, \theta_{t+1}^{i+}) + \omega_t^i \quad \omega_t^i \sim N(0, \Sigma_t^x) \quad \forall \quad Q_t = \Sigma_{t+1}^x \quad (13)$$

$$282 \quad \hat{y}_{t+1}^i = h(x_{t+1}^{i-}, \theta_{t+1}^{i+}) + v_{t+1}^i \quad v_{t+1}^i \sim N(0, \Sigma_{t+1}^y) \quad \forall \quad R_{t+1} = \Sigma_{t+1}^y \quad (14)$$

283 Model states ensemble is similarly updated as follows:

$$284 \quad x_{t+1}^{i+} = x_{t+1}^{i-} + K_{t+1}^x (y_{t+1}^i - \hat{y}_{t+1}^i) \quad (15)$$

$$285 \quad y_{t+1}^i = \hat{y}_{t+1}^i + v_{t+1}^i \quad v_{t+1}^i \sim N(0, R_{t+1}) \quad \forall \quad R_{t+1} = \Sigma_{t+1}^y \quad (16)$$

286 where $K_{t+1}^x \in \mathbb{R}^{m \times n}$ is the Kalman gain for correcting the state trajectories and is obtained by:

$$287 \quad K_{t+1}^x = \Sigma_{t+1}^{xy} [\Sigma_{t+1}^{yy} + R_{t+1}]^{-1} \quad (17)$$

288 where $\Sigma_{t+1}^{xy} \in \mathbb{R}^{m \times n}$ is the cross-covariance matrix of states ensemble and prediction ensemble
 289 (Eq. 16).

$$290 \quad \Sigma_{t+1}^{xy}(s, j) = \frac{1}{N} \sum_{i=1}^N [(x_{t+1}^{i-}(s) - E[x_{t+1}^-(s)]) (\hat{y}_{t+1}^i(j) - E[\hat{y}_{t+1}(j)])] \quad (18)$$

$$291 \quad E[x_{t+1}^-] = \frac{1}{N} \sum_{i=1}^N x_{t+1}^{i-} \quad (19)$$

292 In this study the water depth along the channel is the only state variable ($m=1$). The channel
 293 roughness and bathymetry are two model parameters ($l=2$) and three point source observations



294 including water discharge at gauge 1 and 2 as well as water stage at gauge 2 ($n=3$) are assimilated
295 into the LISFLOOD-FP model (Table 1). Therefore, the Kalman gains used to update the model
296 parameters and states (Eqs 5 and 15) are 2×3 and 1×3 matrices that take advantage of a
297 multivariate point source assimilation while considering the downstream correlation between
298 discharge observations and the correlation between water stage and discharge at gauge 2. **3.3.**

299 **Experimental design**

300 The ultimate goal of this study is to simulate the Hurricane Harvey flood and generate probabilistic
301 flood inundation maps through the DA-hydrodynamic modeling framework. Figure. 1 illustrates
302 the flowchart of the proposed probabilistic flood inundation mapping approach. In this study, the
303 EnKF is performed based on an ensemble size of 100. The boundary conditions including four
304 upstream flows, seven lateral fluxes, and downstream flows are perturbed with adding white noises
305 sampled from a normal distribution with a mean zero and relative error of 20%. The errors are
306 assumed heteroscedastic meaning that their values are proportional to the flow magnitude. To
307 characterize uncertainty in the initial condition, namely water depth, we add a white noise with a
308 mean zero and standard deviation of 1 meter. In this study, using the proposed EnKF-based
309 multivariate assimilation approach, three point-scale observations, i.e., discharge at USGS gauges
310 1 and 2, as well as water stage at gauge 2, are incorporated into the LISFLOOD-FP model to rectify
311 its state variables and parameters, and hence provide more accurate and reliable flood inundation
312 maps. All these three observations are perturbed by adding a normally distributed white noise with
313 a mean zero and a relative error of 20%. First, the LISFLOOD-FP model is forced with the
314 upstream, downstream and lateral flow ensembles. To initialize the state variables in the system,
315 the simulated water depth values at the ending day of the warm-up period (the initial condition for
316 the first day of the model simulation) are perturbed with adding a white noise with a mean zero

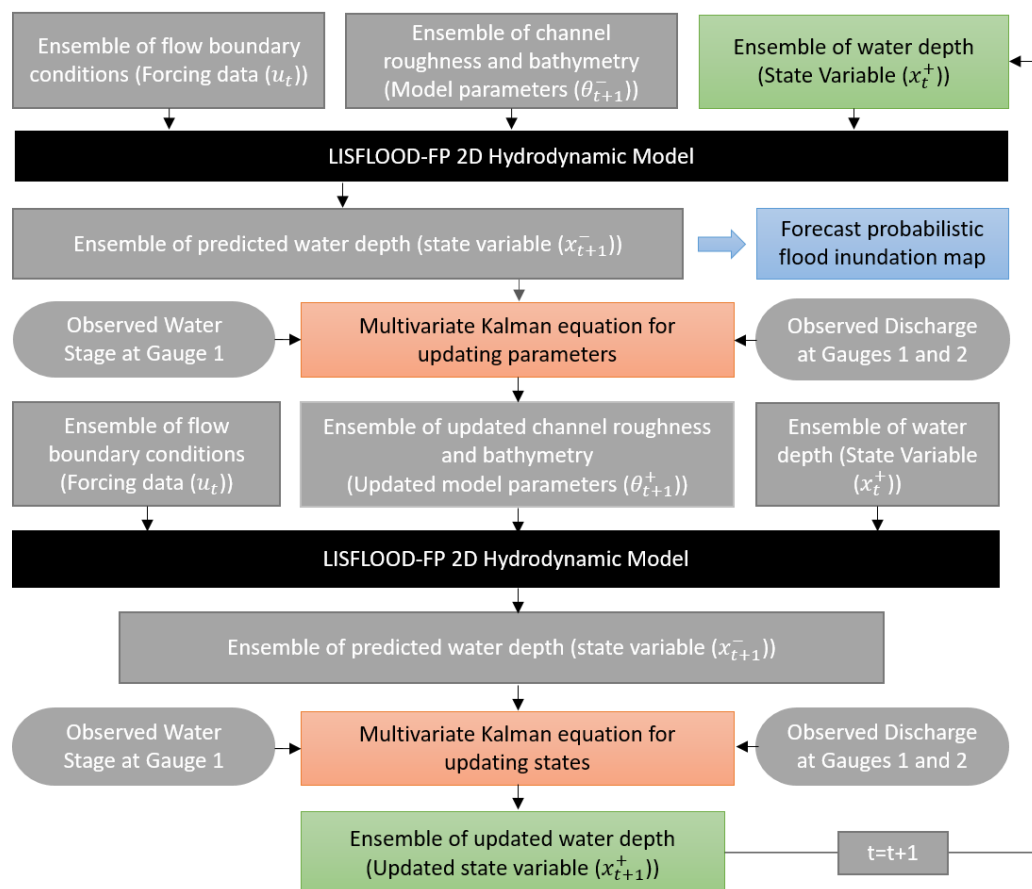


317 and standard deviation of 1 meter. The model parameters (i.e., channel roughness and bathymetry)
318 are initialized using the Latin Hypercube Sampling method and evolved during the assimilation
319 process. The ensemble of water depth values predicted by the model for the next time step together
320 with observations, namely water stage and discharge at gauges are used in the multivariate Kalman
321 equation to update the model parameters. The LISFLOOD-FP model is run for the second time
322 with the updated parameters and the second multivariate Kalman equation uses the predicted water
323 depth with observations to update the ensemble of water depth in the system. The ensemble of
324 updated water depth (state), bathymetry, and channel roughness (parameters) will be used within
325 the LISFLOOD-FP to predict an ensemble of water depth for the next time step. The predicted
326 water depth is simply converted to a probabilistic flood inundation map. Using this data
327 assimilation framework, we can generate 1-day forecast of probabilistic flood inundation maps
328 which would be highly beneficial for real-time flood warning and decision making. It is worth
329 mentioning that the forecasted probabilistic maps account for different sources of uncertainty
330 including the forcing data (boundary condition flows), model parameters (channel roughness and
331 bathymetry), and initial conditions (water depth).

332 The simulation period of the LISFLOOD-FP model is set up for 45 days from July-30-2017 to
333 Sep-12-2017 and the entire month of July is used as a warm-up period. The water depth generated
334 for the end of July will be used as the initial condition of the model. To account for the uncertainty
335 of channel roughness and bathymetry, we sample them from uniform distributions ranging from
336 [0,0.1] and [39,42] m, respectively. The bathymetry parameter is the elevation of the channel bed
337 at the upper location of the channel. The offset parameter is calculated by subtracting this value
338 from DEM at the upper location. Then, the bathymetry vector that includes the channel bed
339 elevation for all channel cells is generated by subtracting the offset from DEM values along the



340 channel. It should be noted that the range of uniform distribution is chosen based on previous
 341 studies (Aronica et al., 2002b; Bales and Wagner, 2009; Di Baldassarre et al., 2009; Horritt, 2006;
 342 Pappenberger et al., 2008), expert judgment, and trial-and-error.



343

344 *Figure 2. Schematic of the DA-hydrodynamic modeling framework for real-time probabilistic*
 345 *flood inundation mapping. The green boxes represent the state variables where their updated*
 346 *values are fed into the LISFLOOD-FP model and provide a probabilistic flood inundation map*
 347 *at the forecast mode (blue box). The black boxes highlight the physical model and the orange*
 348 *boxes represent the Kalman equations used for updating the parameter and state variables by*
 349 *the EnKF.*

350 To assess the effectiveness and robustness of the proposed assimilation framework for
 351 probabilistic flood inundation mapping, we design three different experiments. First, an open-loop



352 (OL) simulation is established where the model is run without assimilation. In the second
353 experiment, we perform DA-hydrodynamic modeling on a synthetic case study where we assume
354 the model is perfect and has no error. In this approach, we set the model parameters (channel
355 roughness and bathymetry), initial state (water depth) and boundary condition flows to fixed values
356 and run the model to generate discharge and water surface elevation across the gauges within the
357 study area. These predicted values are assumed as benchmark observations. This synthetic analysis
358 ensures that the assimilation process performs well and the model parameters end up converging
359 to predefined values. In the next step, we implement the proposed assimilation framework on a
360 real case study where the observed discharge and water surface elevation data that are recorded
361 from the USGS gauges during Hurricane Harvey, are assimilated into the model. Considering the
362 severe flood condition during the Hurricane, we aim to investigate the extent to which the
363 multivariate DA-Hydrodynamic modeling framework improves the model simulation and flood
364 inundation mapping skill.

365 **3.4 Validation strategy**

366 As mentioned before, the convergence of uncertain model parameters toward truth in the
367 synthetic experiment demonstrates the performance of DA-hydrodynamic modeling framework.
368 To provide a robust analysis of each assimilation run, it is necessary to assess the model
369 performance through multiple deterministic (KGE and RMSE) and probabilistic (NRR and
370 Reliability) measures. The summary of performance measures used in this study is tabulated in
371 Table 1.

372

373



374 Table 1: Summary of performance measures used in this study

Performance Measure	Mathematical Representation
Kling-Gupta Efficiency (KGE)	$1 - \sqrt{\left(\left(\frac{\text{Cov}_{y_t y'_t}}{\sigma \sigma'}\right) - 1\right)^2 + \left(\left(\frac{\sigma'}{\sigma}\right) - 1\right)^2 + \left(\left(\frac{\mu'}{\mu}\right) - 1\right)^2}$
Root Mean Square Error (RMSE)	$\sqrt{\frac{1}{T} \sum_{t=1}^T (y'_t - y_t)^2}$
Normalized Root-Mean-Square Error Ratio (NRR)	$\sqrt{\frac{1}{T} \sum_{t=1}^T (y_t - \overline{y'_{\bullet,t}})^2} \times \left(\frac{1}{T} \left\{ \sum_{t=1}^T \sqrt{\frac{1}{T} \left[\sum_{t=1}^T (y_t - \overline{y'_{\bullet,t}})^2 \right]} \right\} \sqrt{\frac{N+1}{2N}}\right)^{-1}$
Reliability	$1 - \frac{2}{T} \sum_{t=1}^T \left \frac{Z_t}{T} - U_t \right $

375

376 y_t and y'_t are the observed and simulated values, respectively. The Kling–Gupta Efficiency (KGE)
 377 varies from $-\infty$ to 1, such that a value of 1 indicates a perfect fit between observed and simulated
 378 values. The pairs of (μ, σ) and (μ', σ') represent the first two statistical moments (means and
 379 standard deviations) of y_t and y'_t , respectively. Root mean squared error (RMSE) is the square
 380 root of the mean of the square of all of the error between the predicted and observed values.

381 NRR (DeChant and Moradkhani, 2012) is calculated to measure the ensemble spread and assess
 382 how confidently the ensemble mean is statistically distinguishable from the ensemble spread.
 383 Reliability (Renard et al., 2010) is a measure of the fit of the Q-Q quantile plot to a uniform. A
 384 value of 1 is exactly uniform and a value of 0 is the farthest possibility from uniform. For the
 385 description of the z_t and U_t calculation, we refer the readers to Renard et al. (2010).



386 The above four performance measures assess the dynamic behavior of DA-hydrodynamic
387 modeling framework at two specific points. Moreover, to spatially evaluate the behavior of the
388 proposed framework, we compare the maximum probabilistic flood inundation maps (union of
389 probabilistic maps over the simulation period) with the observed floodplain map delineated
390 aftermath of Harvey. The Receiver Operating Characteristic (ROC) graph is a common tool for
391 validating probabilistic classifiers (Fawcett, 2006). Consider a deterministic flood map as a binary
392 map where one and zero represent flooded and non-flooded cells, respectively. First, a threshold
393 in the range of [0,1] is used to convert the probabilistic map to a binary deterministic map. This
394 means all cells with the probability of inundation less than a given threshold are converted to zero
395 and other cells are set to one. The binary map is compared with the reference map and the rate of
396 true positive (rtp) and false positive (rfp) are calculated using Equations 7 and 8 (Jafarzadegan and
397 Merwade, 2017):

$$398 \quad rtp = \frac{\text{True positive instances}}{\text{total positives}} \quad (7)$$

$$399 \quad rfp = \frac{\text{False positive instances}}{\text{total negative}} \quad (8)$$

400 where true and false positive instances represent the total number of flooded cells in the reference
401 map that are predicted as flood and non-flooded cells, respectively. Total positives and negatives
402 are total flooded and non-flooded cells in the reference map. This process is repeated and a set of
403 points (rfp.rtp) are generated corresponding to different thresholds. The ROC graph connects the
404 points in the rfp-rtp space and the area under the curve (AUC) represents the performance of the
405 probabilistic classifier (Fawcett, 2006). In this study, we use AUC to compare the performance of
406 OL simulation with the EnKF for probabilistic flood inundation mapping. In addition, we calculate



407 the Underprediction and Overprediction Flood Indices (UFI and OFI) introduced by Jafarzadegan
408 et al., (2018) for comparing probabilistic flood maps against deterministic reference maps:

$$409 \quad UFI = \frac{\sum_{i=1}^N (1-P_i)}{N} \times 100 \quad i \in F \quad (9)$$

$$410 \quad OFI = \frac{\sum_{j=1}^M (P_j)}{M} \times 100 \quad j \in NF \quad (10)$$

411 where F and NF denote the flooded and non-flooded regions in the reference map, and i and j are
412 indicators of cells located within these regions. N and M are the total number of cells in the F and
413 NF regions and P_i , P_j denote the probability of inundation for cells i and j derived from the
414 probabilistic flood maps.

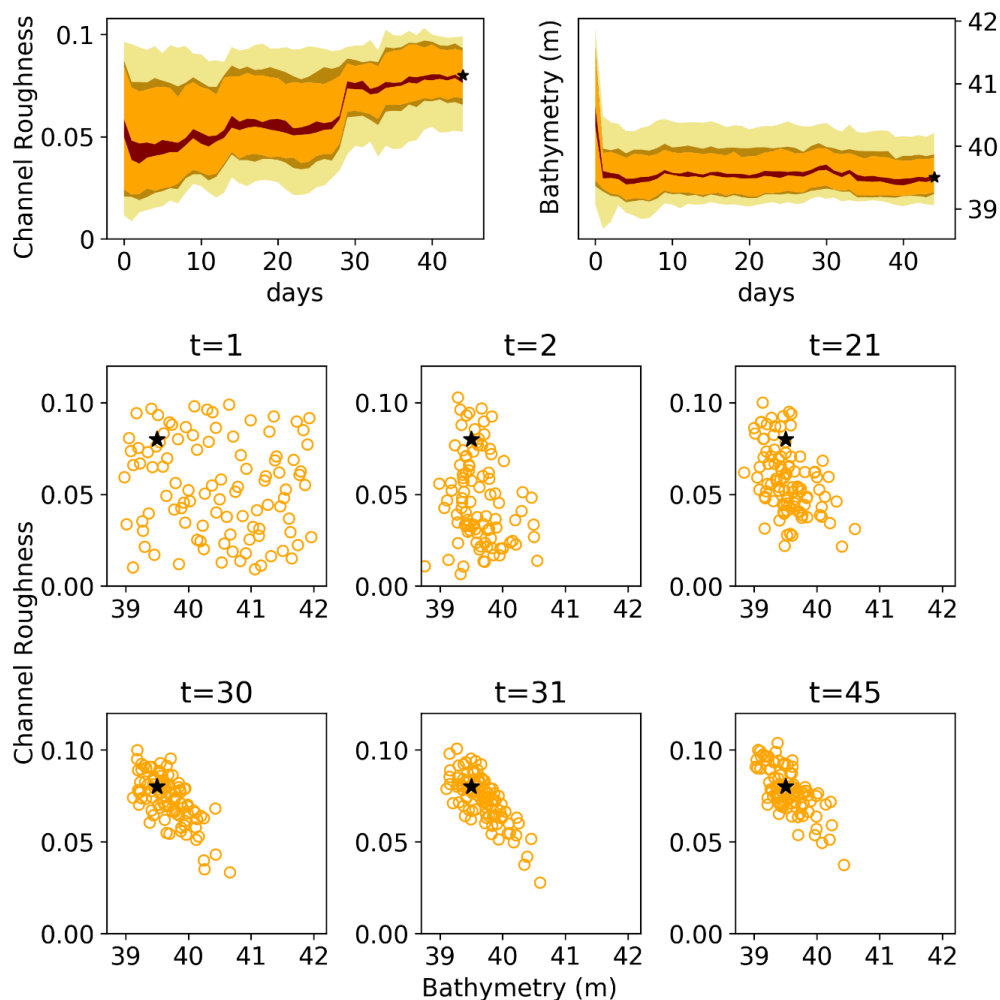
415 **4. Results**

416 **4.1 Synthetic Case Study**

417 We conduct the synthetic experiment to ensure the usefulness and effectiveness of the proposed
418 DA-hydrodynamic modeling framework. Figure 3 presents uncertainty bound evolution of the
419 parameters in the LISFLOOD-FP model (i.e., channel roughness and bathymetry) for 45 days
420 assimilation of synthetic observations (i.e., discharge at gauges 1 and 2 and water stage at gauge
421 2). The shaded areas correspond to 95, 75, 68, and 10 percentile predictive intervals, and the black
422 stars at the end of each parameter subplot represent the true parameter values. As seen both
423 parameters converge smoothly to the certain region in parameter space where the uncertainty
424 bounds stabilize. While the uncertainty bound associated with the bathymetry becomes stabilized
425 at the early stage of the assimilation process, for the channel roughness, the uncertainty bound gets
426 stabilized toward the end of the assimilation period. It is also evident from Figure 3 that the



427 bathymetry is a more identifiable parameter as it shows the fastest convergence with a minimum
428 degree of uncertainty. However, the channel roughness is less identifiable with the slowest
429 convergence. The scatter plots illustrate the evolution of parameter space at six different time
430 segments. The first day ($t=1$) includes all 100 ensemble members of parameters and day 30
431 corresponds to the highest discharge and water stage of flooding when the model parameters reach
432 the highest improvement and get closer to the true value. Figure 3 shows that both model
433 parameters are converging toward the true values as the assimilation proceeds. This indicates the
434 efficacy and usefulness of the proposed DA-hydrodynamic modeling framework developed in this
435 study.



436

437 *Figure 3. Temporal evolution of the LISFLOOD parameters for the synthetic experiment during*
438 *Hurricane Harvey using the EnKF. (a) Temporal evolution of model parameter predictive*
439 *intervals corresponding to 95, 75, 68, and 10 percentile (b) Temporal evolution of particle*
440 *positions in the model parameter space at six different days during the Hurricane.*

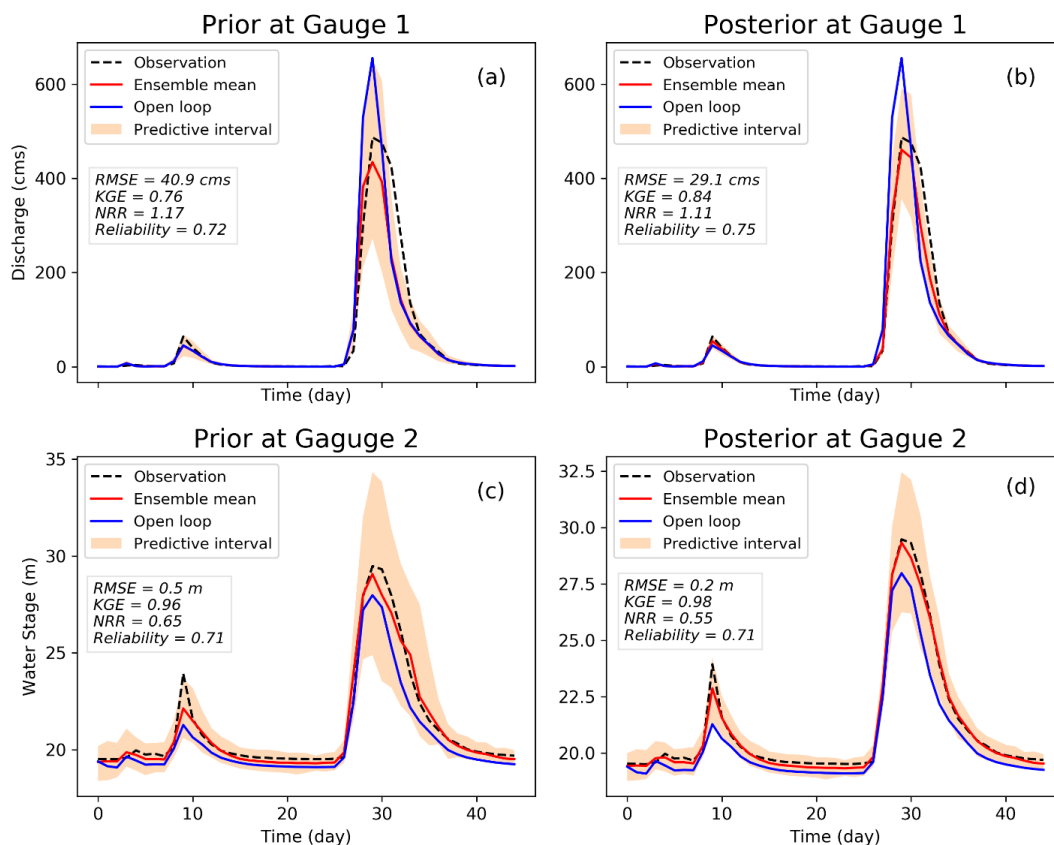
441 **4.2 Real Case Study**

442 In the real experiment, we assimilate the discharge and water stage readings from two internal
443 USGS gauges into the LISFLOOD-FP model. We also run the OL simulation and calculate the
444 ensemble mean to predict the discharge and water stage at these two gauges. Figure 4 presents a



445 comparison of simulated discharge (Figures 4a, 4b) and water stage (Figures 4c, 4d) with
446 observations using both OL and our EnKF-based approach. Figures 4a and 4c are the prior
447 estimates of discharge and water stage, while Figures 4b and 4d show their posteriors which reflect
448 the updated variables after assimilating the observations into the model. It is worth mentioning
449 that although priors represent the results before assimilating new observations into the model, their
450 values are dependent on the initial conditions updated from observations in the previous time step.
451 In this study, since forecasting (1-day lead time) is the main objective of DA-hydrodynamic
452 modeling framework, we specifically focus on behavior of priors. As can be seen, the simulated
453 peak discharge by the OL is highly overestimated by around 200 cms while assimilating the
454 observations improve the results so that their difference with observation is less than 50 cms at the
455 peak of the flood (KGE =0.76 and RMSE=40.9 cms)). In contrast, the simulated water stage in
456 Figures 4c and 4d are underestimated by OL by around 2 meters at the peak. Using the developed
457 approach raises the peak of water stage at peak and reduces the errors significantly (KGE=0.96
458 and RMSE=0.5). The accurate estimates of prior discharge and water stage confirm the
459 applicability of the proposed assimilation framework in forecast mode when real-time flood
460 warning and decision making is the priority. The NRR measure for the prior discharge and water
461 stage are 1.17 and 0.65 showing that the uncertainty bound is underestimated and overestimated,
462 respectively. The reliability of both variables is above 70 percent since the uncertainty bounds
463 encompass the observations for almost the entire simulation period.

464



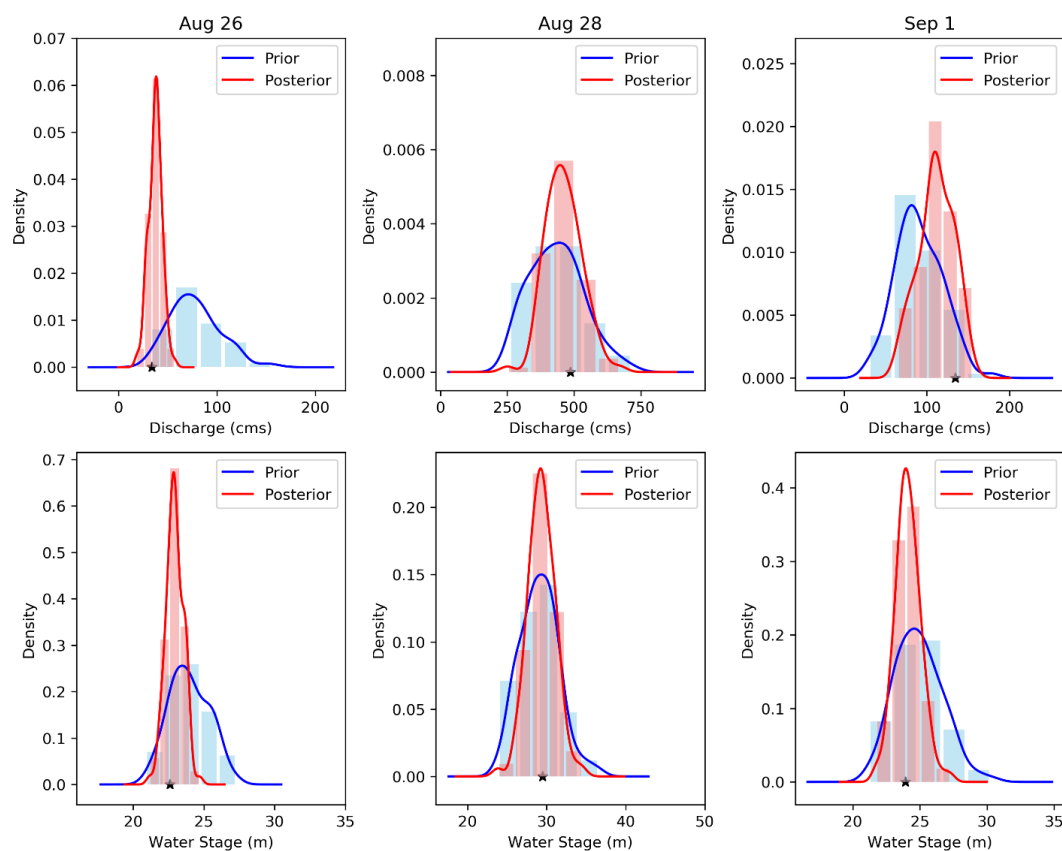
465

466 *Figure 4 Simulation results of LISFLOOD-FP for the real experiment during Hurricane Harvey*
467 *using the EnKF and open-loop. (a) Prior simulated discharge at gauge 1 (b) Posterior simulated*
468 *discharge at gauge 1 (c) Prior simulated water stage at gauge 2 (d) Posterior simulated water*
469 *stage at gauge 2. The shaded areas represent the predictive interval of simulated discharge and*
470 *water stage by EnKF.*

471 Figure 5 illustrates the prior and posterior distributions of discharge and water stage in the
472 beginning, peak, and ending days of Hurricane Harvey flood. In all three days, the uncertainty
473 bounds of both discharge and water stage are narrowed down by assimilating the observations so
474 that posterior distributions are more precise compared to the priors. In the beginning and
475 days (Aug 26 and Sep 1) the mean of prior distributions is substantially shifted toward truth in the
476 posterior distributions. Figure 5 reveals that our developed approach provides more accurate and



477 reliable posterior discharge and water stage distributions compared to prior distributions where the
478 simulations are either overestimated or underestimated. It is noted that, on August 28 (day of flood
479 peak), although the prior distributions accurately represent the observation, they have wide
480 uncertainty bound. After correcting/updated the model state variables and parameters, as posterior
481 distributions show, the uncertainty bound is reduced while the ensemble mean remains closer to
482 the observation.



483

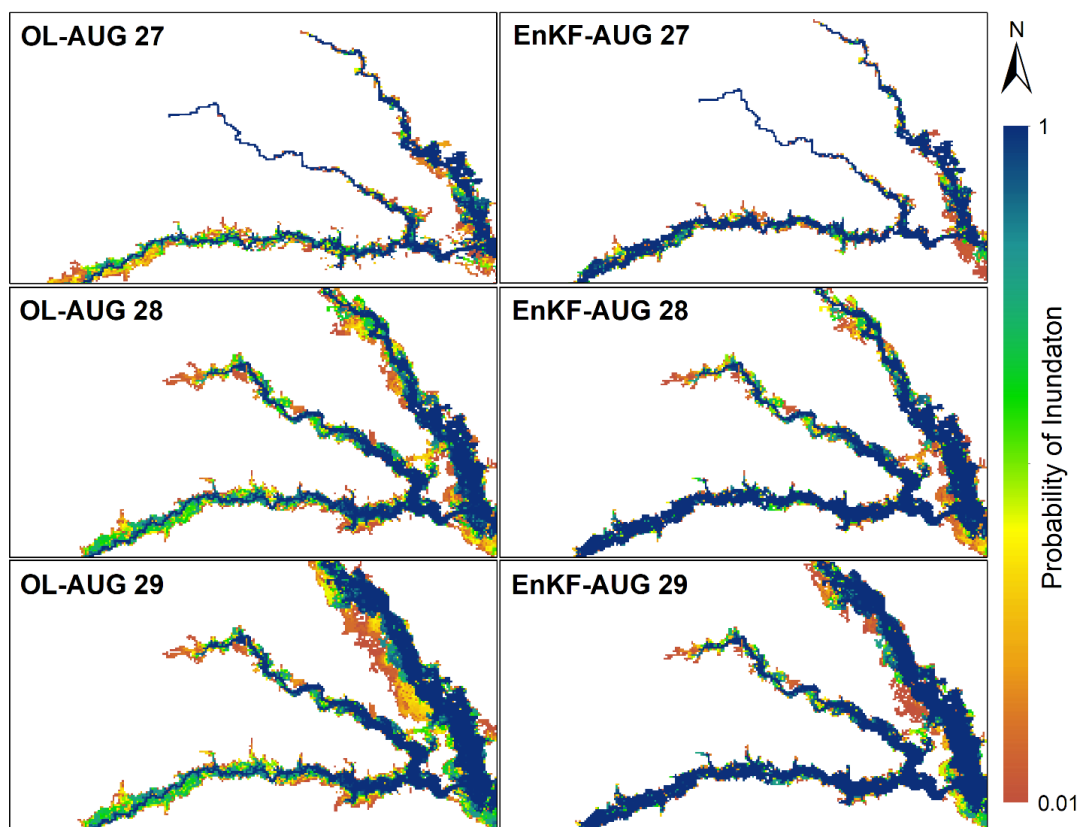
484 *Figure 5. Prior and posterior distribution of discharge (a,b,c) and water stage (c,d,f) at the*
485 *beginning (Aug 26), peak (Aug 28), and ending (Sep1) days of Hurricane Harvey using the*
486 *EnKF*

487



488 **4.3 Probabilistic Flood Inundation Mapping**

489 In this study, we propose a DA-hydrodynamic modeling framework to account for the
490 uncertainties involved in flood modeling and generate real-time probabilistic flood inundation
491 maps. Since the majority of flooding conditions occurred within 6 days from August 27-Sep 1, we
492 display the spatial distribution of water depth in this period and provide probabilistic flood
493 inundation maps using both OL and our developed approach (see Figures 6 and 7). Figure 6
494 represents the first three days of Harvey which corresponds to the upper limb of the flood
495 hydrograph. On August 27, the major difference between the OL and EnKF appears in the regions
496 around the upstream of the lower channel where the EnKF provides a more reliable inundated area.
497 Moving toward the peak of flood on Aug 29, the OL generates a large region of uncertain cells
498 around the banks of the upper channel while both the extent and density of uncertain values in the
499 probabilistic maps generated by the EnKF is smaller during the peak of Harvey.



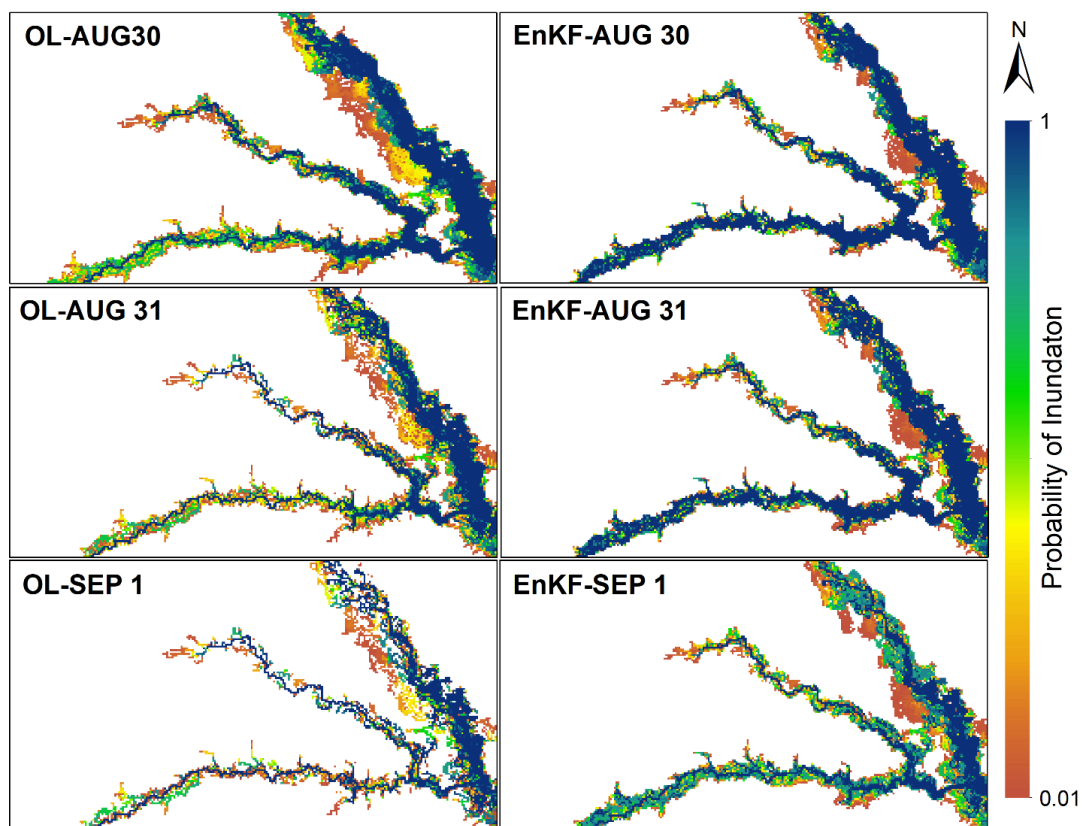
500

501 *Figure 6 Probabilistic flood inundation maps generated by OL and EnKF techniques to simulate*
502 *the upper limb of Harvey flood hydrograph from Aug 27 to Aug 29.*

503 Figure 7 shows the probabilistic inundation areas in the last three days corresponding to the lower
504 limb of the flood hydrograph. In this figure, the discrepancies between the OL and EnKF flood
505 maps increase showing that performing DA is more effective in improving the inundation mapping
506 skill from peak to ending point of the flood hydrograph. A large number of inundated cells
507 generated by the OL are vanished after the peak of Harvey which results in a set of scattered
508 discontinuous maps in Aug 31 and Sep 1. On the other hand, the probabilistic maps generated by
509 the EnKF maintain their continuous shapes so that the probability of inundation is reduced without
510 changing the extent. The merit of the EnKF in improving the flood inundation areas at the lower



511 limb of the flood hydrograph agrees with results in Figures 4c and 4d where the EnKF widens the
512 simulated water stage hydrographs and removes the lag difference that exists between the open-
513 loop and observations.



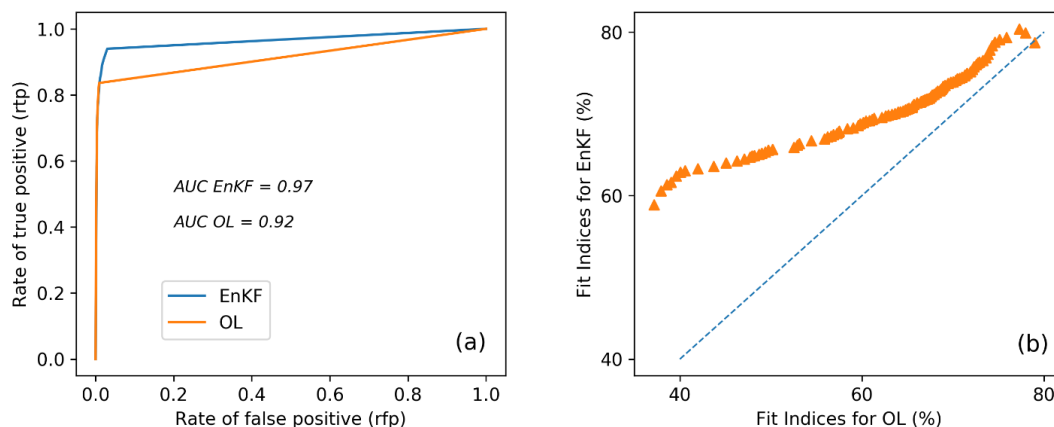
514

515 *Figure 7 Probabilistic flood inundation maps generated by OL and EnKF techniques to simulate*
516 *the lower limb of Harvey flood hydrograph from Aug 30 to Sep 1.*

517 Finally, to quantify the performance of EnKF and OL for generating a spatial distribution of water
518 depth over the domain, we illustrate the ROC graphs, the AUC values, and Fit indices in Figure 8.
519 To calculate these measures, we ignore the temporal distributions and only report the maximum
520 inundation maps that represent the union of flooded areas over the entire period of Harvey.
521 Comparing the EnKF and OL in Figure 8.a, the EnKF line (blue) is closer to the northwest of the



522 rfp-rtp space where its AUC is 5% higher than the OL approach. In Figure 8.b, each point
523 represents the Fit indices for the OL and the EnKF approaches corresponding to a given threshold.
524 Using hundred number of thresholds that each ranging from [0.01,1], the probabilistic maps are
525 converted to 100 deterministic maps and the Fit indices are calculated. The position of scatters
526 above the dash line confirms the EnKF outperforms the OL. In addition to these measures, the
527 [UFI, OFI] indices calculated for OL and EnKF approaches are [30.3, 0.26] %, and [23.4, 0.4]%
528 respectively. The low values of OFI for both approaches ($< 1\%$) show that the simulations mostly
529 underestimate the flood inundation areas. In addition, comparing the indices of both approaches
530 reveal that the EnKF reduces the overall underestimation by around 7%.



531

532 *Figure 8 The Receiver Operating Curves (ROC) indicating the performance of OL and EnKF*
533 *techniques for probabilistic flood inundation mapping*

534 **5. Discussion and Conclusions**

535 The main motivation in this study is to propose a DA-hydrodynamic modeling framework for real-
536 time probabilistic flood inundation mapping. Considering the coarse spatiotemporal resolution of
537 satellite data for capturing the water surface elevation, assimilating them into the hydrodynamic



538 models may not be a practical solution for an upcoming flood event. On the other hand, the
539 availability of daily discharge and water surface elevation data at gauge stations is a great
540 opportunity to establish a multivariate DA-hydrodynamic modeling framework that updates the
541 initial condition of modeling at daily scale and forecast the flood inundation areas at 1 day lead
542 time. Here, we used the EnKF data assimilation method in conjunction with a hydrodynamic
543 model to account for different sources of uncertainties involved in different layers of model
544 simulations, including the boundary conditions, model parameters, and initial condition, and
545 generate real-time probabilistic flood inundation maps. To further enhance the performance of the
546 developed framework, the discharge and water stage at two different gauges are simultaneously
547 assimilated into the LISFLOOD-FP model. The multivariate EnKF approach considers the
548 correlation between discharge at two gauges and between discharge and water surface elevation at
549 one gauge using a modified covariance matrix and Kalman gain equation.

550 In the synthetic experiment, we examined the convergence of model parameters toward truth and
551 found that the proposed DA-hydrodynamic modeling framework can be successfully used to
552 improve the accuracy and reliability of model predictions while accounting for uncertainties
553 associated with model parameters. The channel roughness coefficient varied more rapidly than
554 the bathymetry during the temporal evolutions of these parameters showing the better
555 identifiability of this parameter. The validation results of the real experiment revealed that the
556 assimilation with the EnKF approach improves the model predictions at across temporal and
557 spatial scales (i.e., discharge and water stage time series at gauges and flood maps showing the
558 maximum water depth over the simulation period). These improvements are more pronounced
559 during the falling limb of the flood hydrograph where the EnKF widens the simulated hydrograph
560 and removes the existing lag compared to the observations. Similarly, the simulated flood



561 inundation maps confirm that the OL provides discontinuous scattered maps during the flood
562 recession period while the EnKF provides a more accurate representation of the inundation areas.
563 The validation results also demonstrate that the EnKF reduces the underestimation by 7% and
564 outperformed the OL approach by around 5% for probabilistic flood inundation mapping.

565 To simulate flood hazards during the emergency of an upcoming flood event, using an efficient
566 flood modeling framework is of paramount importance. However, a simplified model setup (i.e.
567 using coarse resolution DEM, assuming uniform roughness coefficient for channel and floodplain,
568 estimating bathymetry by lowering DEM with one parameter) for efficient flood modeling is prone
569 to losing accuracy. Particularly, for an extreme flooding condition such as Hurricane Harvey, the
570 simplified modeling may pose significant errors. The results obtained from the simulation of the
571 real experiment demonstrated that despite using a simplified efficient modeling setup, we can still
572 simulate the discharge, water stage, and inundation areas for an extreme flood event with
573 acceptable accuracy while accounting for uncertainties involved in model predictions. This shows
574 that assimilating the gauge data into a simplified model setup improves the accuracy, and provides
575 an efficient probabilistic framework for real-time flood inundation mapping that considers
576 potential sources of uncertainties in different layers of modeling.

577 The time dependency that exists between the upstream and downstream gauges along a channel
578 can affect the performance of multivariate assimilation with those gauges. For future studies, using
579 a more advanced DA technique that fully characterizes the model structural uncertainty
580 (Abbaszadeh et al., 2019), and considering the time lag dependency between multiple gauges can
581 improve the performance of modeling and provide more realistic assimilation of the hydrodynamic
582 models. Finally, proposing a DA-hydrodynamic modeling framework that considers the DEM and



583 channel width uncertainty can provide a more comprehensive uncertainty quantification for
584 probabilistic flood inundation mapping in future studies.

585 **Data availability**

586 All the data used in this study, including the gauge streamflow and water stage data and the DEMs,
587 are publicly available from the USGS website and National Elevation Dataset (NED). The
588 reference flood maps provided for Hurricane Harvey is available from the USGS report at
589 <https://pubs.usgs.gov/sir/2018/5070/sir20185070.pdf>.

590 **Author contribution**

591 KJ and PA designed the synthetic and real experiments. KJ developed, set up, evaluated and
592 implemented the DA-hydrodynamic modeling framework for both experiments. PA provided
593 inputs on the assimilation part. KJ wrote the first draft of the manuscript. HR and PA edited the
594 manuscript.

595 **Competing interests**

596 The authors declare that they have no conflict of interest.

597 **Acknowledgment**

598 Partial financial support for this study was provided by the USACE contract #W912HZ2020055.
599 We would like to thank the anonymous reviewers for their constructive comments on the original
600 version of the manuscript.

601

602



603 References

- 604 Abbaszadeh, P., Gavahi, K., Moradkhani, H., 2020. Multivariate remotely sensed and in-situ data
605 assimilation for enhancing community WRF-Hydro model forecasting. *Adv. Water*
606 *Resour.* 145, 103721.
- 607 Abbaszadeh, P., Moradkhani, H., Daescu, D.N., 2019. The Quest for Model Uncertainty
608 Quantification: A Hybrid Ensemble and Variational Data Assimilation Framework.
609 *Water Resour. Res.* 55, 2407–2431. <https://doi.org/10.1029/2018WR023629>
- 610 Abbaszadeh, P., Moradkhani, H., Yan, H., 2018. Enhancing hydrologic data assimilation by
611 evolutionary Particle Filter and Markov Chain Monte Carlo. *Adv. Water Resour.* 111,
612 192–204. <https://doi.org/10.1016/j.advwatres.2017.11.011>
- 613 Alemohammad, S.H., McLaughlin, D.B., Entekhabi, D., 2015. Quantifying precipitation
614 uncertainty for land data assimilation applications. *Mon. Weather Rev.* 143, 3276–3299.
- 615 Anderson, J.L., Anderson, S.L., 1999. A Monte Carlo implementation of the nonlinear filtering
616 problem to produce ensemble assimilations and forecasts. *Mon. Weather Rev.* 127, 2741–
617 2758.
- 618 Aronica, G., Bates, P.D., Horritt, M.S., 2002a. Assessing the uncertainty in distributed model
619 predictions using observed binary pattern information within GLUE. *Hydrol. Process.* 16,
620 2001–2016. <https://doi.org/10.1002/hyp.398>
- 621 Aronica, G., Bates, P.D., Horritt, M.S., 2002b. Assessing the uncertainty in distributed model
622 predictions using observed binary pattern information within GLUE. *Hydrol. Process.* 16,
623 2001–2016. <https://doi.org/10.1002/hyp.398>
- 624 Azimi, S., Dariane, A.B., Modanesi, S., Bauer-Marschallinger, B., Bindlish, R., Wagner, W.,
625 Massari, C., 2020. Assimilation of Sentinel 1 and SMAP-based satellite soil moisture
626 retrievals into SWAT hydrological model: The impact of satellite revisit time and product
627 spatial resolution on flood simulations in small basins. *J. Hydrol.* 581, 124367.
- 628 Baldassarre, G.D., Schumann, G., Bates, P., 2009. Near real time satellite imagery to support and
629 verify timely flood modelling. *Hydrol. Process.* 23, 799–803.
630 <https://doi.org/10.1002/hyp.7229>
- 631 Bales, J.D., Wagner, C.R., 2009. Sources of uncertainty in flood inundation maps. *J. Flood Risk*
632 *Manag.* 2, 139–147. <https://doi.org/10.1111/j.1753-318X.2009.01029.x>
- 633 Bates, P.D., De Roo, A.P.J., 2000. A simple raster-based model for flood inundation simulation.
634 *J. Hydrol.* 236, 54–77. [https://doi.org/10.1016/S0022-1694\(00\)00278-X](https://doi.org/10.1016/S0022-1694(00)00278-X)
- 635 Brêda, J.P.L.F., Paiva, R.C.D., Bravo, J.M., Passaia, O.A., Moreira, D.M., 2019. Assimilation of
636 Satellite Altimetry Data for Effective River Bathymetry. *Water Resour. Res.* 55, 7441–
637 7463. <https://doi.org/10.1029/2018WR024010>
- 638 Clark, M.P., Hay, L.E., 2004. Use of Medium-Range Numerical Weather Prediction Model
639 Output to Produce Forecasts of Streamflow. *J. Hydrometeorol.* 5, 15–32.
640 [https://doi.org/10.1175/1525-7541\(2004\)005<0015:UOMNWP>2.0.CO;2](https://doi.org/10.1175/1525-7541(2004)005<0015:UOMNWP>2.0.CO;2)



- 641 Courtier, P., Derber, J., Errico, R.O.N., Louis, J.-F., VukićEvić, T., 1993. Important literature
642 on the use of adjoint, variational methods and the Kalman filter in meteorology. *Tellus*
643 *Dyn. Meteorol. Oceanogr.* 45, 342–357.
- 644 Cuo, L., Pagano, T.C., Wang, Q.J., 2011. A Review of Quantitative Precipitation Forecasts and
645 Their Use in Short- to Medium-Range Streamflow Forecasting. *J. Hydrometeorol.* 12,
646 713–728. <https://doi.org/10.1175/2011JHM1347.1>
- 647 DeChant, C.M., Moradkhani, H., 2014. Toward a reliable prediction of seasonal forecast
648 uncertainty: Addressing model and initial condition uncertainty with ensemble data
649 assimilation and sequential Bayesian combination. *J. Hydrol.* 519, 2967–2977.
- 650 Di Baldassarre, G., Schumann, G., Bates, P.D., 2009. A technique for the calibration of hydraulic
651 models using uncertain satellite observations of flood extent. *J. Hydrol.* 367, 276–282.
652 <https://doi.org/10.1016/j.jhydrol.2009.01.020>
- 653 Domeneghetti, A., Vorogushyn, S., Castellarin, A., Merz, B., Brath, A., 2013. Probabilistic flood
654 hazard mapping: effects of uncertain boundary conditions. *Hydrol. Earth Syst. Sci.* 17,
655 3127–3140.
- 656 Durand, M., Andreadis, K.M., Alsdorf, D.E., Lettenmaier, D.P., Moller, D., Wilson, M., 2008.
657 Estimation of bathymetric depth and slope from data assimilation of swath altimetry into
658 a hydrodynamic model. *Geophys. Res. Lett.* 35.
- 659 Fawcett, T., 2006. An introduction to ROC analysis. *Pattern Recognit. Lett., ROC Analysis in*
660 *Pattern Recognition* 27, 861–874. <https://doi.org/10.1016/j.patrec.2005.10.010>
- 661 García-Pintado, J., Neal, J.C., Mason, D.C., Dance, S.L., Bates, P.D., 2013. Scheduling satellite-
662 based SAR acquisition for sequential assimilation of water level observations into flood
663 modelling. *J. Hydrol.* 495, 252–266. <https://doi.org/10.1016/j.jhydrol.2013.03.050>
- 664 Giustarini, L., Matgen, P., Hostache, R., Montanari, M., Plaza Guingla, D.A., Pauwels, V., De
665 Lannoy, G., De Keyser, R., Pfister, L., Hoffmann, L., 2011. Assimilating SAR-derived
666 water level data into a hydraulic model: a case study. *Hydrol. Earth Syst. Sci.* 15, 2349–
667 2365.
- 668 Gobeyn, S., Van Wesemael, A., Neal, J., Lievens, H., Eerdenbrugh, K.V., De Vleeschouwer, N.,
669 Vernieuwe, H., Schumann, G.J.-P., Di Baldassarre, G., Baets, B.D., Bates, P.D.,
670 Verhoest, N.E.C., 2017. Impact of the timing of a SAR image acquisition on the
671 calibration of a flood inundation model. *Adv. Water Resour.* 100, 126–138.
672 <https://doi.org/10.1016/j.advwatres.2016.12.005>
- 673 Habets, F., LeMoigne, P., Noilhan, J., 2004. On the utility of operational precipitation forecasts
674 to served as input for streamflow forecasting. *J. Hydrol.* 293, 270–288.
675 <https://doi.org/10.1016/j.jhydrol.2004.02.004>
- 676 Hall, J.W., Tarantola, S., Bates, P.D., Horritt, M.S., 2005. Distributed Sensitivity Analysis of
677 Flood Inundation Model Calibration. *J. Hydraul. Eng.* 131, 117–126.
678 [https://doi.org/10.1061/\(ASCE\)0733-9429\(2005\)131:2\(117\)](https://doi.org/10.1061/(ASCE)0733-9429(2005)131:2(117))
- 679 Horritt, M.S., 2006. A methodology for the validation of uncertain flood inundation models. *J.*
680 *Hydrol.* 326, 153–165. <https://doi.org/10.1016/j.jhydrol.2005.10.027>



- 681 Hostache, R., Chini, M., Giustarini, L., Neal, J., Kavetski, D., Wood, M., Corato, G., Pelich, R.-
682 M., Matgen, P., 2018. Near-Real-Time Assimilation of SAR-Derived Flood Maps for
683 Improving Flood Forecasts. *Water Resour. Res.* 54, 5516–5535.
684 <https://doi.org/10.1029/2017WR022205>
- 685 Hostache, R., Lai, X., Monnier, J., Puech, C., 2010. Assimilation of spatially distributed water
686 levels into a shallow-water flood model. Part II: Use of a remote sensing image of Mosel
687 River. *J. Hydrol.* 390, 257–268. <https://doi.org/10.1016/j.jhydrol.2010.07.003>
- 688 Hostache, R., Matgen, P., Schumann, G., Puech, C., Hoffmann, L., Pfister, L., 2009. Water Level
689 Estimation and Reduction of Hydraulic Model Calibration Uncertainties Using Satellite
690 SAR Images of Floods. *IEEE Trans. Geosci. Remote Sens.* 47, 431–441.
691 <https://doi.org/10.1109/TGRS.2008.2008718>
- 692 Hunter, N.M., Bates, P.D., Horritt, M.S., De Roo, A.P.J., Werner, M.G.F., 2005. Utility of
693 different data types for calibrating flood inundation models within a GLUE framework.
694 *Hydrol. Earth Syst. Sci. Discuss.* 9, 412–430.
- 695 Jafarzadegan, K., Merwade, V., 2017. A DEM-based approach for large-scale floodplain
696 mapping in ungauged watersheds. *J. Hydrol.* 550, 650–662.
697 <https://doi.org/10.1016/j.jhydrol.2017.04.053>
- 698 Jafarzadegan, K., Merwade, V., Saksena, S., 2018. A geomorphic approach to 100-year
699 floodplain mapping for the Conterminous United States. *J. Hydrol.* 561, 43–58.
700 <https://doi.org/10.1016/j.jhydrol.2018.03.061>
- 701 Kumar, S.V., Dong, J., Peters-Lidard, C.D., Mocko, D., Gómez, B., 2017. Role of forcing
702 uncertainty and background model error characterization in snow data assimilation.
703 *Hydrol. Earth Syst. Sci.* 21, 2637–2647.
- 704 Lai, X., Liang, Q., Yesou, H., Daillet, S., 2014. Variational assimilation of remotely sensed flood
705 extents using a 2-D flood model. *Hydrol. Earth Syst. Sci.* 18.
- 706 Leach, J.M., Kornelsen, K.C., Coulibaly, P., 2018. Assimilation of near-real time data products
707 into models of an urban basin. *J. Hydrol.* 563, 51–64.
- 708 Lee, H., Seo, D.-J., Koren, V., 2011. Assimilation of streamflow and in situ soil moisture data
709 into operational distributed hydrologic models: Effects of uncertainties in the data and
710 initial model soil moisture states. *Adv. Water Resour.* 34, 1597–1615.
- 711 Lievens, H., Reichle, R.H., Liu, Q., De Lannoy, G.J., Dunbar, R.S., Kim, S.B., Das, N.N., Cosh,
712 M., Walker, J.P., Wagner, W., 2017. Joint Sentinel-1 and SMAP data assimilation to
713 improve soil moisture estimates. *Geophys. Res. Lett.* 44, 6145–6153.
- 714 Maidment, D.R., 2017. Conceptual Framework for the National Flood Interoperability
715 Experiment. *JAWRA J. Am. Water Resour. Assoc.* 53, 245–257.
716 <https://doi.org/10.1111/1752-1688.12474>
- 717 Mason, D.C., Bates, P.D., Dall’Amico, J.T., 2009. Calibration of uncertain flood inundation
718 models using remotely sensed water levels. *J. Hydrol.* 368, 224–236.
- 719 Matgen, P., Montanari, M., Hostache, R., Pfister, L., Hoffmann, L., Plaza, D., Pauwels, V.R.N.,
720 De Lannoy, G., De Keyser, R., Savenije, H.H.G., 2010a. Towards the sequential



- 721 assimilation of SAR-derived water stages into hydraulic models using the Particle Filter:
722 proof of concept. *Hydrol. Earth Syst. Sci.* 14, 1773–1785.
- 723 Matgen, P., Montanari, M., Hostache, R., Pfister, L., Hoffmann, L., Plaza, D., Pauwels, V.R.N.,
724 De Lannoy, G., De Keyser, R., Savenije, H.H.G., 2010b. Towards the sequential
725 assimilation of SAR-derived water stages into hydraulic models using the Particle Filter:
726 proof of concept. *Hydrol. Earth Syst. Sci.* 14, 1773–1785.
- 727 Merwade, V., Cook, A., Coonrod, J., 2008. GIS techniques for creating river terrain models for
728 hydrodynamic modeling and flood inundation mapping. *Environ. Model. Softw.* 23,
729 1300–1311. <https://doi.org/10.1016/j.envsoft.2008.03.005>
- 730 Moradkhani, H., Hsu, K.-L., Gupta, H., Sorooshian, S., 2005a. Uncertainty assessment of
731 hydrologic model states and parameters: Sequential data assimilation using the particle
732 filter. *Water Resour. Res.* 41.
- 733 Moradkhani, H., Nearing, G.S., Abbaszadeh, P., Pathiraja, S., 2019. Fundamentals of data
734 assimilation and theoretical advances. *Handb. Hydrometeorol. Ensemble Forecast.*
735 Springer Berl. Heidelb. Berl. Heidelb. 675–699.
- 736 Moradkhani, H., Sorooshian, S., Gupta, H.V., Houser, P.R., 2005b. Dual state–parameter
737 estimation of hydrological models using ensemble Kalman filter. *Adv. Water Resour.* 28,
738 135–147. <https://doi.org/10.1016/j.advwatres.2004.09.002>
- 739 Munier, S., Polebistki, A., Brown, C., Belaud, G., Lettenmaier, D.P., 2015. SWOT data
740 assimilation for operational reservoir management on the upper Niger River Basin. *Water*
741 *Resour. Res.* 51, 554–575. <https://doi.org/10.1002/2014WR016157>
- 742 Neal, J., Keef, C., Bates, P., Beven, K., Leedal, D., 2013. Probabilistic flood risk mapping
743 including spatial dependence. *Hydrol. Process.* 27, 1349–1363.
744 <https://doi.org/10.1002/hyp.9572>
- 745 Neal, J., Schumann, G., Bates, P., 2012. A subgrid channel model for simulating river hydraulics
746 and floodplain inundation over large and data sparse areas. *Water Resour. Res.* 48.
747 <https://doi.org/10.1029/2012WR012514>
- 748 Neal, J., Schumann, G., Bates, P., Buytaert, W., Matgen, P., Pappenberger, F., 2009. A data
749 assimilation approach to discharge estimation from space. *Hydrol. Process.* 23, 3641–
750 3649. <https://doi.org/10.1002/hyp.7518>
- 751 Pappenberger, F., Beven, K.J., Ratto, M., Matgen, P., 2008. Multi-method global sensitivity
752 analysis of flood inundation models. *Adv. Water Resour.* 31, 1–14.
753 <https://doi.org/10.1016/j.advwatres.2007.04.009>
- 754 Pappenberger, F., Frodsham, K., Beven, K., Romanowicz, R., Matgen, P., 2007. Fuzzy set
755 approach to calibrating distributed flood inundation models using remote sensing
756 observations. *Hydrol. Earth Syst. Sci. Discuss.* 11, 739–752.
- 757 Pathiraja, S., Moradkhani, H., Marshall, L., Sharma, A., Geenens, G., 2018. Data-driven model
758 uncertainty estimation in hydrologic data assimilation. *Water Resour. Res.* 54, 1252–
759 1280.



- 760 Pauwels, V.R., Hoeben, R., Verhoest, N.E., De Troch, F.P., 2001. The importance of the spatial
761 patterns of remotely sensed soil moisture in the improvement of discharge predictions for
762 small-scale basins through data assimilation. *J. Hydrol.* 251, 88–102.
- 763 Pedinotti, V., Boone, A., Ricci, S., Biancamaria, S., Mognard, N., 2014. Assimilation of satellite
764 data to optimize large-scale hydrological model parameters: a case study for the SWOT
765 mission. *Hydrol. Earth Syst. Sci.* 18, 4485–4507. [https://doi.org/10.5194/hess-18-4485-](https://doi.org/10.5194/hess-18-4485-2014)
766 2014
- 767 Pedrozo-Acuña, A., Rodríguez-Rincón, J.P., Arganis-Juárez, M., Domínguez-Mora, R.,
768 Villareal, F.J.G., 2015. Estimation of probabilistic flood inundation maps for an extreme
769 event: Pánuco River, México. *J. Flood Risk Manag.* 8, 177–192.
770 <https://doi.org/10.1111/jfr3.12067>
- 771 Pinter, N., Santos, N., Hui, R., 2017. Preliminary analysis of Hurricane Harvey flooding in
772 Harris County, Texas. Retrieved UC Davis Cent. Watershed Sci.-Calif. WaterBlog
773 [Https://californiawaterblog
774 Com20170901preliminary-Anal.--Hurricaneharvey-Flooding--
775 Harris-Cty.-Tex.](https://californiawaterblog.com/2017/09/01/preliminary-anal.-hurricane-harvey-flooding-harris-cty-tex/)
- 775 Purvis, M.J., Bates, P.D., Hayes, C.M., 2008. A probabilistic methodology to estimate future
776 coastal flood risk due to sea level rise. *Coast. Eng.* 55, 1062–1073.
777 <https://doi.org/10.1016/j.coastaleng.2008.04.008>
- 778 Rahman, Md.R., Thakur, P.K., 2018. Detecting, mapping and analysing of flood water
779 propagation using synthetic aperture radar (SAR) satellite data and GIS: A case study
780 from the Kendrapara District of Orissa State of India. *Egypt. J. Remote Sens. Space Sci.*,
781 *EJRS Special Issue: Microwave Remote Sensing in honor of Professor Adel Yehia 21*,
782 S37–S41. <https://doi.org/10.1016/j.ejrs.2017.10.002>
- 783 Reichle, R.H., McLaughlin, D.B., Entekhabi, D., 2002. Hydrologic data assimilation with the
784 ensemble Kalman filter. *Mon. Weather Rev.* 130, 103–114.
- 785 Renard, B., Kavetski, D., Kuczera, G., Thyer, M., Franks, S.W., 2010. Understanding predictive
786 uncertainty in hydrologic modeling: The challenge of identifying input and structural
787 errors. *Water Resour. Res.* 46. <https://doi.org/10.1029/2009WR008328>
- 788 Romanowicz, R., Beven, K., 2003. Estimation of flood inundation probabilities as conditioned
789 on event inundation maps. *Water Resour. Res.* 39.
790 <https://doi.org/10.1029/2001WR001056>
- 791 Sheffield, J., Pan, M., Wood, E.F., Mitchell, K.E., Houser, P.R., Schaake, J.C., Robock, A.,
792 Lohmann, D., Cosgrove, B., Duan, Q., Luo, L., Higgins, R.W., Pinker, R.T., Tarpley,
793 J.D., Ramsay, B.H., 2003. Snow process modeling in the North American Land Data
794 Assimilation System (NLDAS): 1. Evaluation of model-simulated snow cover extent. *J.*
795 *Geophys. Res. Atmospheres* 108. <https://doi.org/10.1029/2002JD003274>
- 796 Slater, A.G., Clark, M.P., 2006. Snow data assimilation via an ensemble Kalman filter. *J.*
797 *Hydrometeorol.* 7, 478–493.



- 798 Tarpanelli, A., Brocca, L., Melone, F., Moramarco, T., 2013. Hydraulic modelling calibration in
799 small rivers by using coarse resolution synthetic aperture radar imagery. *Hydrol. Process.*
800 27, 1321–1330. <https://doi.org/10.1002/hyp.9550>
- 801 Teng, J., Jakeman, A.J., Vaze, J., Croke, B.F.W., Dutta, D., Kim, S., 2017. Flood inundation
802 modelling: A review of methods, recent advances and uncertainty analysis. *Environ.*
803 *Model. Softw.* 90, 201–216. <https://doi.org/10.1016/j.envsoft.2017.01.006>
- 804 Vrugt, J.A., Gupta, H.V., Nualláin, B., Bouten, W., 2006. Real-time data assimilation for
805 operational ensemble streamflow forecasting. *J. Hydrometeorol.* 7, 548–565.
- 806 Yoon, Y., Durand, M., Merry, C.J., Clark, E.A., Andreadis, K.M., Alsdorf, D.E., 2012a.
807 Estimating river bathymetry from data assimilation of synthetic SWOT measurements. *J.*
808 *Hydrol.* 464, 363–375.
- 809 Yoon, Y., Durand, M., Merry, C.J., Clark, E.A., Andreadis, K.M., Alsdorf, D.E., 2012b.
810 Estimating river bathymetry from data assimilation of synthetic SWOT measurements. *J.*
811 *Hydrol.* 464, 363–375.
- 812 Zhang, Q., Shi, L., Holzman, M., Ye, M., Wang, Y., Carmona, F., Zha, Y., 2019. A dynamic
813 data-driven method for dealing with model structural error in soil moisture data
814 assimilation. *Adv. Water Resour.* 132, 103407.
- 815
- 816
- 817
- 818
- 819
- 820